A Fully Automatic Method to Extract Rare Earth Mining Areas from Landsat Images

Some of the authors of this publication are also working on these related projects:

Unified satellite image fusion View project

shape reconstruction View project

A fully automatic method to extract rare earth mining areas from Landsat Images

Bo Wu, Chaoyang Fang, Le Yu, Xin Huang, and Qiang Zhang

Abstract

This paper proposes a new morphological mining feature index (MMFI) by synthesizing multi-scale and multi-direction differential morphological profiles (DMPs) to effectively separate REMAs from other land covers with similar spectral signals and local brightness contrast. The MMFI enhances the local brightness contrast of REMAs by highlighting the morphological characteristics of REMA structure, and improves the identification of roads and bare soil, which have similar spectral signatures to REMAs. Moreover, a new threshold optimization method that maximizes the histogram entropy is presented, whereby REMAs can be automatically extracted from the MMFI image without sample collection and machine learning. Therefore, it is a fully automatic method suitable for REMA extraction over large areas. To validate the proposed method, three temporal Landsat images acquired at Changting County, China, were used to extract REMA information. Our results demonstrate that the proposed method can achieve good classification accuracy compared with other methods.

Keywords: Rare earth mining area (REMA); mining feature index; differential morphological profiles; histogram entropy.

Bo Wu and Qiang Zhang are with key lab of spatial data mining and information sharing of ministry of education, Fuzhou University, China {wavelet778@sohu.com};
Chaoyang Fang is with state key laboratory of Poyang lake wetland and watershed research, ministry of education, Jiangxi normal university, Nanchang, China;
Le Yu is with the ministry of education key laboratory for earth system modeling, center for earth system science, Tsinghua University, Beijing, 100084, China;
Xin Huang is with the School of remote sensing and information engineering, Wuhan University 129, Luoyu road, Wuhan, 430079, China.

Introduction

China, known as the "kingdom of rare earths", is among the world's leading countries in terms of rare earth resources, producing over 90% of the world supply in recent years (China National Bureau of Statistics, 2010). A large and rapid increase in the extraction and use of rare earth elements (REE) has occurred in recent years; however, the use of simple mining techniques and inadequate supervision of local government has caused substantial increases in the contamination levels of soil and water around the mining areas (Olias et al., 2005; Miao et al., 2011; Li et al., 2013). Therefore, monitoring rare earth mining areas (REMAs) and their dynamics in a timely and cost-effective manner is highly desirable for environmental agencies and policy makers, as it can provide a scientific base for integrated pollution control and ecological remediation of contaminated environment.

Satellite-based earth observations record synoptic and repetitive data over very large areas. The acquired images, particularly those of the Landsat Thematic Mapper/Enhanced Thematic Mapper plus (TM/ETM+) and Advanced Spaceborne Thermal Emission and Reflection Radiometer (ASTER) are a valuable data source for mapping assemblages of alteration minerals (Crosta and Moore, 1989; Rowan and Mars, 2003; Mars et al., 2011; Pour and Hashim, 2012), such as iron oxides, clay, and alunite, that occur in hydrothermally altered rocks, especially in inaccessible areas (Rowan and Mars, 2003; Chen et al., 2007). Each land cover type has a diagnostic spectral response that can be generally identified from satellite images; this constitutes the theoretical basis of land cover mapping and classification. The spectrum of the reflected energy can be determined from the image brightness; using spectral analysis we can then identify objects in the image. In practice, however, the brightness is influenced by several factors including atmospheric effects, the spectral and spatial resolution of the image, sub-pixel level heterogeneity in the

chemical and mineralogical composition of the rock, and the presence of soil, vegetation cover, and surface weathering (Yu et al., 2011). Therefore, for efficient lithological or mining classification, texture information is usually extracted from remote sensing data, adding additional features to the dataset (e.g. Li et al., 2009; Yu et al., 2012). The textual features are essential information for image classification, because they provide important clues for identifying homogeneous land cover in complex regions.
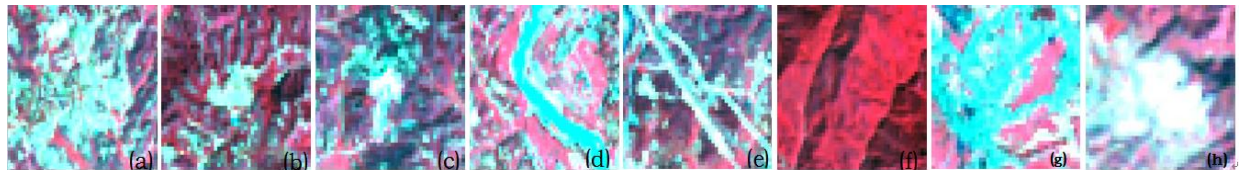

Plate 1 Images of some typical land covers in false-color composited image. From left to right: (a) pond leaching REMA, (b) in-situ leaching REMA, (c) in-situ heap leaching REMA, (d) water, (e) road, (f) vegetation, (g) settlement, and (h) bare land.

To extract REMAs, image features such as the spectrum, shape, and texture of the land cover are required. Plate 1 shows examples of typical land covers in the study area. Mining activities create features that can be observed in remotely sensed images, which provide distinctive information for detecting the REMA. Basically, there are three commonly used methods for distilling iron-based rare earth ore in south China, i.e. the in-situ leaching method, pond leaching method, and in-situ heap leaching method, all of which inevitably cause vegetation deterioration. For example, the image of the site where in-situ leaching was used (Plate 1) shows a pattern of stripes (high-density points) along the mountain ridge. In contrast, the images of the in-situ leaching site and pond leaching site show large areas of vegetation deterioration.

Because REMAs in southern China are found mostly in rugged mountain areas, the spectra of the land covers are strongly affected by the terrain; therefore, spectral-based classification of land cover is unreliable. Accordingly, in this study we focused our analysis on determining effective image textural features for REMA target identification. Some commonly used spatial texture features include wavelet texture (Ouma et al., 2006), the gray-level co-occurrence matrix (GLCM) (Myint et al., 2004),

3

morphological profiles (Pesaresi and Benedifsson, 2001; Fauvel et al., 2008), and fractal texture (Li et al.,

2014); some of these are used for REMA mapping (Peng et al., 2013; Li et al., 2014). However, many of

these algorithms refer to the supervised approaches, where a large number of training samples are needed

to model the distribution of various land-cover categories. As seen in Plate 1, REMAs are often associated

with vegetation deterioration that produces high local contrast; therefore, the local contrast of the GLCM

and the directional components of the textural signal need to be considered. Recently, Huang and Zhang

(2012) developed the morphological building index (MBI) for automatic identification of buildings in high

spatial resolution imagery. The basic idea of MBI is to establish a relationship between the image implicit

characteristics and the morphological features to enhance the algorithm's ability to recognize land covers

with similar spectral signals and local contrast. The MBI can be automatically calculated without sample

collection or machine learning; therefore, it is suitable for updating and monitoring REMA dynamics.

Based on the work of Huang and Zhang (2012), this paper proposes the morphological mining feature

index (MMFI) that captures contextual information to help distinguish between the spectral signature of

REMAs and those of other land covers.

In this study we propose a fully automatic yet efficient REMA extraction method from Landsat images.

Specifically, the MMFI is synthesized by multi-scale and multi-direction differential morphological

profiles (DMPs) by applying a series of mathematical morphological opening and closing operations, and

then the MMFI is automatically extracted by threshold segmentation. Note that although the use of DMPs

to extract buildings in urban areas from high spatial resolution images has been extensively studied

(Benediktsson et al., 2003; Jin and Davis, 2005; Huang and Zhang, 2011, 2012), to the best of our

knowledge, this is the first time that the DMPs technique is introduced to depict the local contrast of bright

structures for rare earth ore recognition from Landsat images. However, to adapt the DMP (or MBI) for REMA extraction, two improvements were made: 1) A band ratio parameter is integrated into the average DMPs to emphasize and quantify the spectral differences between REMA and bare soil, because they share a similar spectral response. 2) A multiple-criteria threshold selecting method is used to better separate the REMA from other background objects.

The rest of this paper is organized as follows. In Section 3 we formulate the morphological MMFI and present the proposed extraction framework for REMA. The experimental results are shown in Section 4 with three temporal TM images, and section 5 concludes the paper.

The proposed methodology

Spectral analysis

The basic goal of the MMFI is to provide a measure of the separation between REMA and other land covers with similar spectral responses and local contrast by depicting the implicit spectral and structural characteristics. Instead of finding the maximum of the multispectral bands for each pixel to synthesize a single bright band, we conducted a spectral profile analysis on typical land covers to learn which band has the maximum brightness. Six typical ground classes, i.e. road (263 pixels), water (201 pixels), vegetation (378 pixels), bare land (33 pixels), settlement (243 pixels), and REMA (172 pixels) were randomly selected in the image acquired from Landsat 8 operational land imager (OLI), and their average spectral profiles with maximum, mean and minimum (max-mean-min) values are plotted in Fig. 2, where zones of REMA that can be easily confused with other land covers are shaded gray.
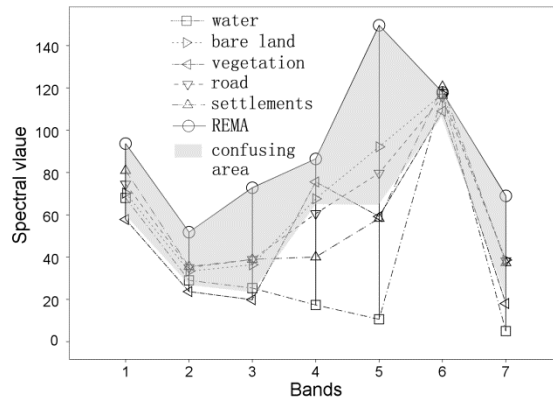
Fig.1 Spectral profiles represented by the mean of six typical land covers in the study area, based on the image at Changting County, southeastern China

The REMA spectral signature has the highest digital number in the SWR band (TM 5), and displays strong brightness in all the other bands. On the other hand, some land covers, i.e., water body, vegetation, and rural areas have lower values in the TM5 band. REMAs are often surrounded by vegetation (Plate 1); therefore, the SWR band produces a high local contrast for REMAs, producing distinctive DMP features. Although there are still some overlapping zones between REMAs and roads, bare land, and bright vegetation, it is however the most useful band for building DMPs. Therefore, we used an SWR band (TM5) to construct the DMPs and applied the MMFI to the remote sensing data to separate the REMA from other land covers.

Building the MMFI feature

In Fig.1, the grey zone represents the spectral zone where discrimination between REMA and other land covers is difficult, especially in the case of bare land, roads, and bright vegetation. In this zone, distinguishing REMA from other land covers cannot be achieved reliably with only spectral signatures. Accordingly, extraction of the textual information is required to complement the spectral feature space. Therefore, we introduce morphological operators to extract the DMP features at multiple scales and directions to enhance bright structures and local pixel contrast, and then generate the MMFI feature image.

6

The MMFI is expected to reveal multi-scale relationships between the implicit characteristics of REMA and the morphological operators, such that REMAs can be effectively extracted by setting a threshold on the MMFI feature image. It should be emphasized that the proposed MMFI was basically based on the DMP and MBI techniques. The related concepts of morphological profile and the DMP can be readily referred the literatures (Pesaresi and Benediktsson, 2001; Benediktsson et al., 2003), and the details of using the DMP to construct the MBI were in references (Huang and Zhang, 2011, 2012). For the clarity and conciseness, we only summary the basic procedures of building MMFI, but do not intend to delineate the details of DMP and MBI methods. Readers can refer these references for details.

Step 1 Defining the structural elements

A fundamental step for the use of DMP method is to design the shape and size as a filtering operator, known as the structural element (SE), which acts as a probe for extracting or suppressing specific image structures by checking that each position of the SE fits within the image objects. In our case, the road and bare soil are the two most difficult land covers to be separated from REMAs because they are also brighter than their neighboring pixels and have similar spectral characteristics to those of REMA. However, roads usually appear on the image as linear features with one or two main directions, whereas REMAs normally appear as irregular polygons with isotropic shapes. Since a single-SE size approach appears not to suitable for complex structures, the MMFI feature image is implemented on a series of linear structural elements to form DMPs, such that the size and directionality of the land cover structures are captured. To this aim, the linear structure element is defined as $se = \mathrm{strelan}(d, s)$, parameterized by two parameters d and s, which represent the direction and scale of the operating structure respectively.

Step 2 White top-hat transform (WTHT) by reconstruction

Generally, the opening/closing operator can isolate the bright/dark structures in images where the objects are brighter/darker than the surrounding features in images. In this sense, the opening operation helps to separate REMAs from bare roads despite their similar spectral characteristics. In order to isolate features with a thinner support than a given SE, it is a common practice to use a top-hat morphological transform by taking the residual of the opening, closing and original images for a better shape preservation (Benediktsson et al., 2003). The WTHT reconstruction operation is formulated by subtracting the opening operation from the initial image on the same image.

$$WTH(d,s) = TM5 - \gamma_{TM5}(se) \tag{1}$$

where $\gamma_{TM5}(se)$ denotes the opening of the image by reconstruction of the TM5 band image, and WTH is the WTHT performed by reconstruction with the linear structural element se with the scale s and direction d parameters. However, Eq. (1) may remove the small REMA objects because the morphological opening operator can remove bright objects smaller than se and smooth the boundary of larger objects. To remedy this problem, we first perform the image closing reconstruction and then the WTHT reconstruction.

$$WTH(d,s) = Tb - \gamma_{Tb}(se) \tag{2}$$

where $Tb = \phi_{TM5}(se)$ is the output image by performing a closing operator to the TM5 band, and $\gamma_{Tb}(se)$ is the opening operator of the Tb image. Because the closing operator can suppress the darker small objects and join adjacent objects together, we argue that replacing TM5 by Tb can improve the homogeneity of an object while leaving its geometry unaffected for structures larger than se.

Step 3 Differential morphological profiles (DMPs)

Since some structures may have a high response for a given SE size, and a lower response for other SE

sizes, depending on the interaction between the SE size and the size of the structures, it is a good idea to use different linear structuring elements. As a result, series of WTHT features can then be produced by varying the parameters of scale s and direction d. To make full use of the WTHT features, the residues of two successive filtering operations, were used to build the DMPs. We adopted DMP is because it has the ability to preserve the thin, enveloped or small objects in images (Pesaresi and Benediktsson, 2001), which benefits the extraction of REMAs. The DMP features calculate the residue for two successive scales in the same direction.

$$DMP(d,s) = |WTH(d,(s + \Delta s)) - WTH(d,s)| \tag{3}$$

where Δs represents the scale parameter with an interval $s_{\min} \leq \Delta s \leq s_{\max}$, which can normally be determined by the spatial resolution and the size of the image. By varying d and Δs, series of DMP features were generated. Note that we did not extract the DMPs for the direction parameter because the WTHT reconstruction operation was insensitive to it.

Step 4 Construction of the MMFI

The REMA and bare soil or low-density vegetation (Fig.1) have similar spectral responses and spatial structural characteristics, which makes it difficult to distinguish between them even when using DMPs. To mitigate the problem, we applied a band ratio operator to relief terrain effect and reflect the bare soil characteristic (Sabins, 1999), and integrated it into DMP to help discriminate between REMAs and bare land. Hence, the morphological mine feature index (MMFI) was finally formulated as:

$$MMFI = \frac{1}{n} \sum_{i=1}^{n} DMP(d,s) - \lambda \ Ratio. \tag{4}$$

The band ratio is defined as $Ratio = MIR/NIR$, where MIR and NIR are the short-wavelength-infrared and near-infrared bands, respectively, $n = d \times s$ denotes the total number of DMPs, and λ indicates the

bare land adjusting factor. The rationality of constructing MMFI is based on the fact that REMA structures have larger values in most directions of the WTHT DMP histogram since they show high local contrast in these directions. Thus, REMAs often correspond to larger MMFI values.

Determining the threshold

Once the MMFI image is generated, the REMA can then be extracted by applying an optimizing threshold. There are many thresholding methods can be selected for MMFI image segmentation, such as the maximal intra-classes variance proposed by Otsu (1979) and histogram entropy (Kapur and Shaoo, 1985). In this paper, the histogram entropy method (HEM) was basically selected for MMFI segmentation for its simplicity and robustness, which obtains the optimal threshold by maximizing the a priori entropies of the object and the background classes. However, because the MMFI feature image were dominated by complex backgrounds, the REMAs only accounting for a small potion. Therefore, we determined the optimal threshold with the histogram entropy method by simultaneously imposing Otsu and the uniform criteria (Levine and Nazif, 1985), such that both the gray-level distribution and the spatial information of MMFI were used. Assuming that t^* is the optimal threshold to segment MMFI into class A and B, such that A and B reach the total maximum entropy, i.e. $\mathrm{E}_f = E_A + E_B = -\mathrm{p}_A \ln(\mathrm{p}_A) - (1-p_A)\ln(1-p_A)$, where $p_A = \sum_{i=0}^{t} p_i$; t_1 and t_2 denote the threshold optimized by Otsu and the uniform criteria, respectively, we then obtained the optimal threshold t^* as following,

$$\mathrm{t}^* = \begin{cases} \max(t_1, t_2), & if \ \ \mathrm{p}_A(t_1), \mathrm{p}_A(t_2) \in [0, 0.5] \\ \min(t_1, t_2), & if \ \ \mathrm{p}_A(t_1), \mathrm{p}_A(t_2) \in [0.5, 1] \\ \mathrm{p}_A(t^*) = 0.5, & if \ \ (p_A(t_1) - 0.5)(p_A(t_2) - 0.5) < 0 \end{cases} \tag{5}$$

Experimental results and analysis

MMFI feature image analysis

The research area, in Changting County, was within the latitude range of 25°18′40″–26°02′05″N, and longitude range 116°00′45″–116°39′20″E, covering an area of about 3090 km². It is a mountainous area located in southwestern Fujian Province on the eastern edge of Jiangxi Province. The area has complex geological structure and contains abundant mining resources, especially rare earth deposits. It ranks as the richest rear earth in Fujian province, hence a good study area for our experiments.
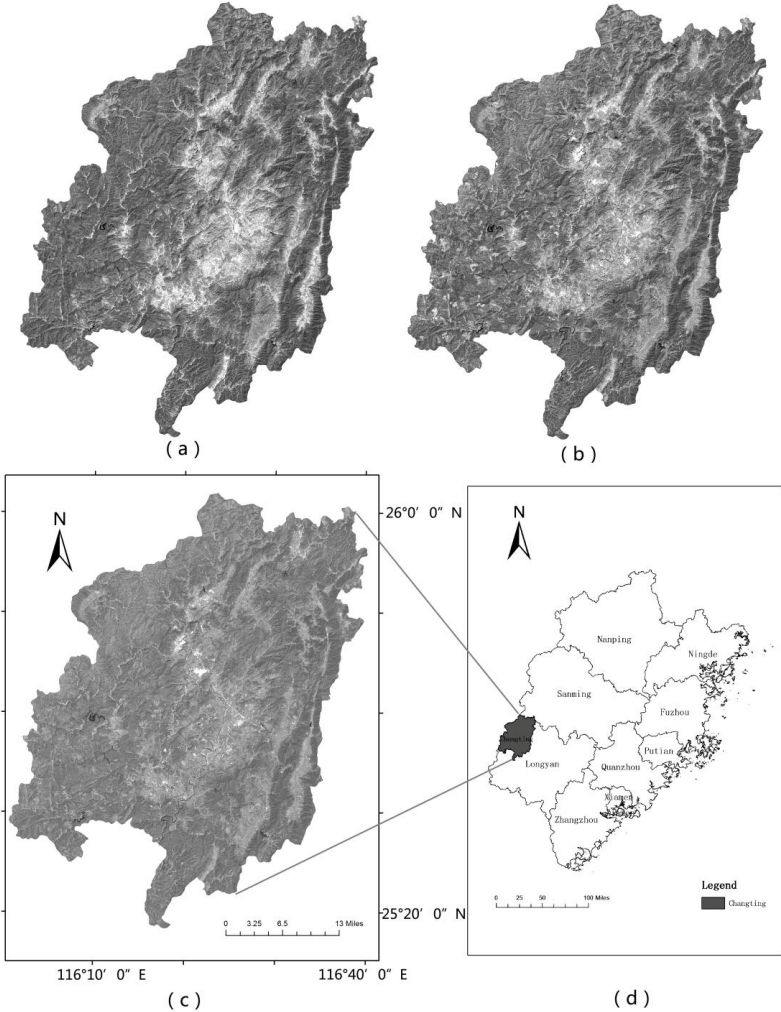

Fig.2 Illustrating three TM/ETM+/OLI images of the study area for band 4, acquired in 2003, 2010, and 2013

Three temporal TM/ETM+/OLI images, acquired on 26 October 2003, 29 October 2010, and 4 October 2013 respectively, were analyzed to validate the effectiveness of the proposed method. The images were all geo-referenced with a spatial resolution of 30 m, and each corrected pixel of the output image has the same WGS-84 coordinates. Fig.2 shows the three temporal images with band 4.

Based on Li et al. (2013) and our field investigation in 2013, the highest concentrations of REMAs in Changting County are in the towns of Hetian and Sanzhou towns. Therefore, we assessed our proposed method of extracting MMFI to the area around Hetian town with about size of 300*300 pixels in the OLI image acquired at 2013. The linear structural elements in our algorithm extend in four directions, namely $0°$, $45°$, $90°$, and $135°$, and each direction is associated with 11 scales ($s_{min}=2$, $s_{max}=12$, $\Delta s=1$) to generate the WTHT feature image. Examples of focused area are shown in Fig. 3.
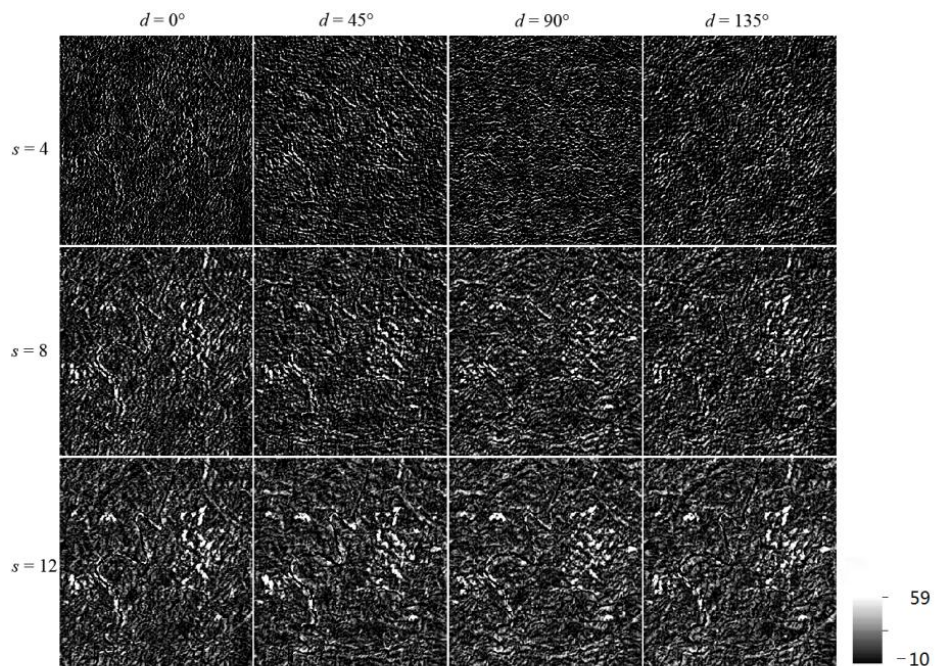

Fig. 3 Morphological WTHT features of different scale and directions

The REMAs appear brighter than other land covers, indicating that REMAs can be significantly enhanced by extracting the morphological WTHT features. Moreover, the WTHT reconstruction can detect

small brightness structures by suppressing the dark background. The differences among the WTHT images of different directions are relatively minor (Fig. 3), indicating that the directional parameter does not have a significant effect on the morphological WTHT. In contrast, the differences of WTHT generated by varying the scale are more significant, suggesting that scale s is the most important parameter. Therefore, we extracted the DMP features each time from the WTHT with two different scales and only one direction.
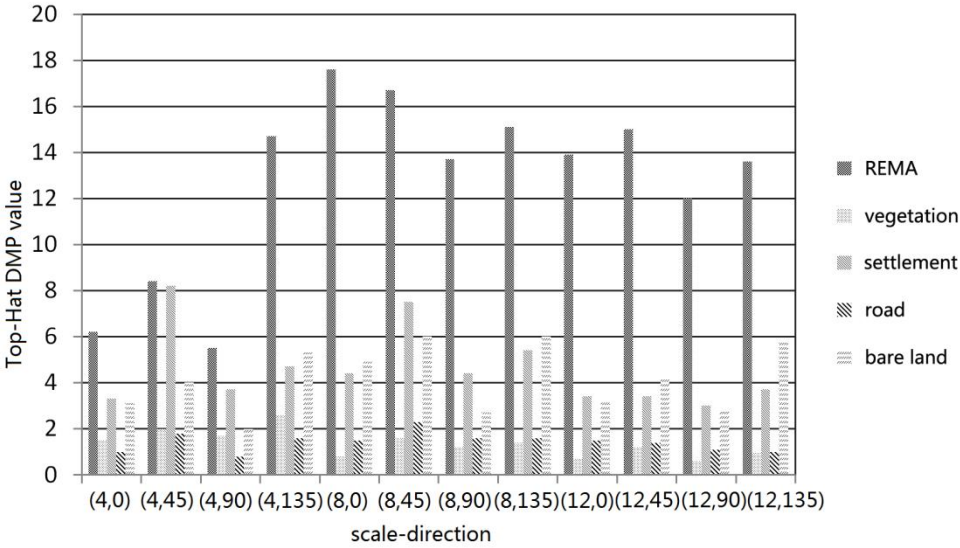

Fig. 4 The DMP values of five typical land covers

To make full use of the local contrast information, the average DMPs for the five typical land covers, i.e. rare earth minerals, vegetation, urban area, roads, and bare land, were derived as shown in Fig. 4, where the horizontal axis displays the scale and direction parameters; thus, (4, 0) denotes $s = 4$ and $d = 0^\circ$. The samples were randomly selected, with the number of samples for the five land covers mentioned above being 404, 578, 414, 203, and 257, respectively. The average DMPs show quite different features, especially the REMA ones, which have values higher than 6 in all 12 profiles, and are larger than the DMP values of the other four classes. In contrast, the DMP values in the vegetation and rural areas are very low in all the profiles, indicating they can be easily separated from the REMAs based on a threshold value. The

REMAs can be distinguished from roads and bare land areas with most parameter combinations, such as the DMPs with parameters (4, 135), (8, 0), (8, 45), (8, 90), (8, 135), (12, 0), (12, 45), and (12, 90), due to the significant difference between their DMP values and those of REMAs. However, the average DMPs produced by parameters (4, 0), (4, 45), and (4, 90) display only minor differences between the various land covers because of their similar spectral signatures, which implies that some land covers can be easily confused with REMAs.
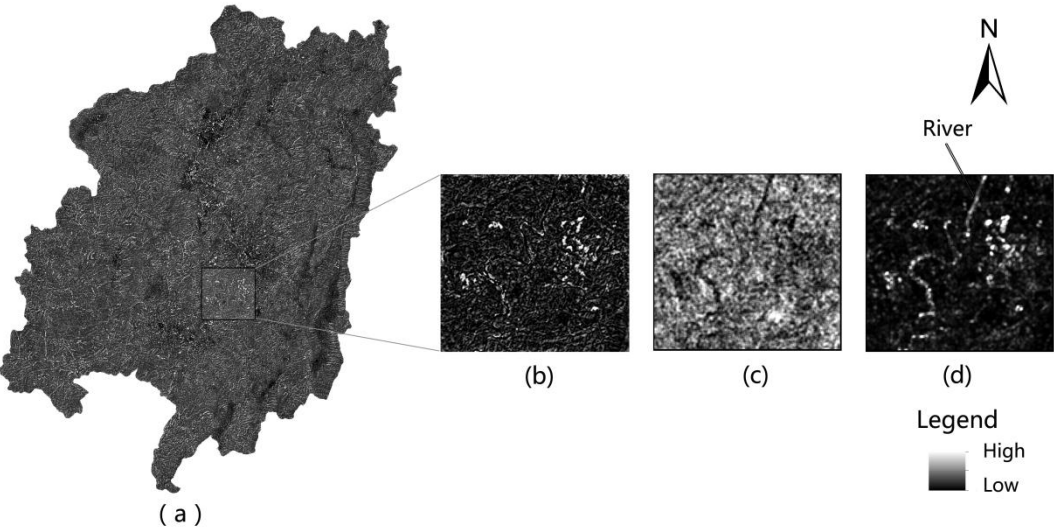

Fig. 5 Comparison of some extracted image features. (a) MMFI for Changting County; (b) MMFI for focused area; (c) Homogeneity by GLCM; and (d) Contrast by GLCM.

The final MMFI image of Changting County and the focused area are shown in Fig. 5a and 5b, respectively. The REMAs have higher values (white areas) in the MMFI image, whereas the other land covers are black or gray because of their lower values. It can also be observed that the edges of the REMA objects are clear. However, some linear objects, such as roads and the sand along the Ting River also have relative high values, indicating that some additional extracting operations are required to remove confused land covers in the extraction processing. For comparison, two other texture features, homogeneity and

contrast, extracted from GLCM with 5×5 window size are illustrated in Fig. 5c and 5d, respectively. It is clear that the homogeneity feature does not capture the REMA characteristics (see black areas). In contrast, the contrast feature is in accord to the MMFI feature, but their edges of the REMA objects are inaccurate. As a result, the MMFI feature has more powerful ability to accurately separate the REMA form background.

Extraction of REMA

The MMFI pixel distribution graph and its associated accumulated histogram are shown in Fig. 6a and 6b, respectively. It can be seen that the MMFI image does not follow a Gaussian normal distribution. Most of the MMFI pixels values are lower than 2; with increasing MMFI values, the probability of occurrence decreases. The enlarged insert (up-right area in Fig. 6a) shows the MMFI pixel distribution range of 3.5–6.5. The curve in Fig. 6b represents the accumulated values of the MMFI image, and Fig. 6(c) illustrates the relationship between the accumulated distribution probability and the total histogram entropy. The thresholds selected by Otsu and the uniform criteria method are 3.563 and 3.704, and the associated probability distribution of the two thresholds are 0.823 (right vertical line, Fig. 6c) and 0.894 (left vertical line, Fig. 6c), respectively. The condition of Eq. (5) is satisfied if the threshold suggested by Otsu (1979) is used to optimize the threshold criteria, with a total entropy of 0.467.
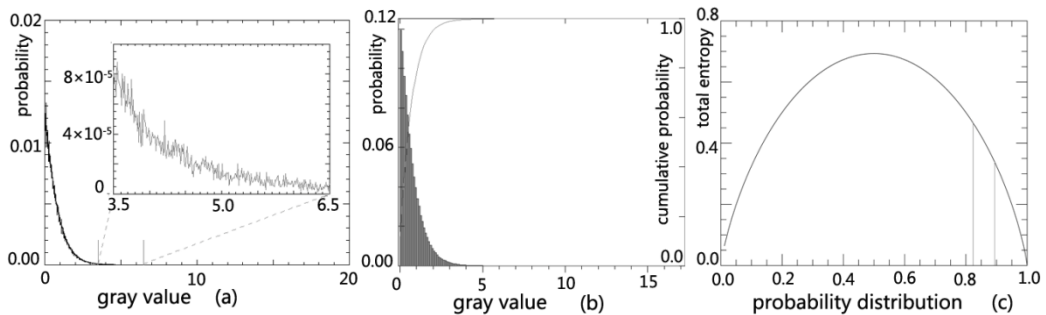

Fig. 6 Probability graphs of MMFI image results. (a) MMFI pixel distribution, (b) accumulated

histogram of MMFI, (c) relationship between accumulated distribution and the total histogram entropy

Table 1 The optimal threshold for the MMFI feature image

Criterion	Threshold	Probability	Total entropy
Otsu t_1	3.563	0.823	0.467
consistent t_2	3.704	0.894	0.338
Proposed t^*	3.563	0.823	0.467

Since some land covers, such as bare soil, roads, and very bright vegetation, have similar spectral reflectance and local brightness contrast, they also exhibit high values in MMFI feature. As a result, the extracted REMA may still contain other land covers when the single threshold is applied. To reduce this error, we implemented additional extracting rules to refine the extracted the REMA result. The normalized difference vegetation index (NDVI) and bare soil index (BSI) are good indictors to extract vegetation and soil classes, respectively. Therefore, we used these two indices to indicate vegetation and bare soil. Moreover, sand and detritus along the river show similar spectral and morphological structure as REMA (Fig. 5). To correct these false positive results a buffer operation along the river was conducted by introducing the normalized difference water index (NDWI) which provides indication for river identification. The NDVI, BSI, and NDWI are defined as follows,

$$NDVI = \frac{\rho_{nir} - \rho_{red}}{\rho_{red} + \rho_{nir}} \tag{6}$$

$$BSI = \frac{[(\rho_{mir1} + \rho_{red}) - (\rho_{nir} + \rho_{blue})]}{[(\rho_{mir1} + \rho_{red}) + (\rho_{nir} + \rho_{blue})]} \tag{7}$$

$$NDWI = \frac{\rho_{green} - \rho_{nir}}{\rho_{green} + \rho_{nir}} \tag{8}$$

where ρ_{mir1}, ρ_{nir}, ρ_{red}, ρ_{green}, and ρ_{blue} indicate the reflectance of the SWR (TM5), NIR (TM4), Red (TM3), Green (TM2), and blue (TM1) bands, respectively. Combining all the indices, REMA extraction can be refined by using the following criteria:

$$FFMI > t_m \;\; \&\& \;\; NDVI < t_a \;\; \&\& \;\; BSI < t_b \;\; \&\& \;\; Buffer(river) > t_p, \tag{9}$$

where t_m is the threshold automatically determined by the proposed method, and t_a, t_b, and t_p are predefined as 0.2, 0.05, and 5. The REMAs can then be extracted by applying the condition $FFMI > 3.563$ and the result is refined by an "if–then" logic calculation by applying three additional conditions: NDVI<0.2, BSI<0.05, and $Buffer(river) > 5$ pixels to reduce false readings from bare soil, low density vegetation, and sand.

Fig. 7a shows the REMAs identified by manual interpretation with the help of high spatial images (WorldView-2 and ZY-3). Fig. 7b shows the REMAs extracted from the MMFI image generated using the threshold $t_1 = 3.563$. In this image other land covers, such as soil and the sand along the Ting River banks, appear as REMAs. Fig. 7c shows the REMAs extracted using the combined criteria, which on the whole agrees with the referenced map. It can be visually found that the mismatch areas are lying in the border of objects, indicating that a refinement can be obtained with post-processing method (Huang, et al, 2014).
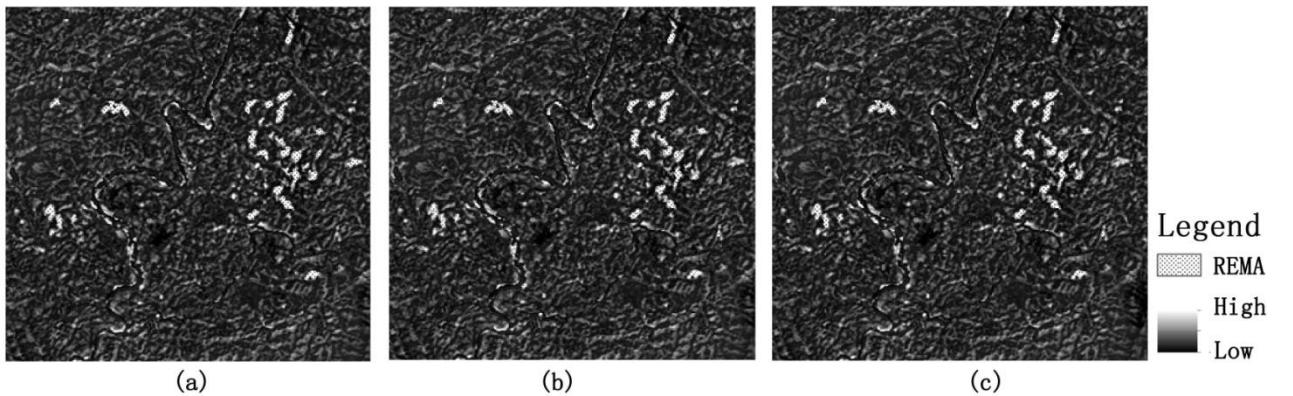

Fig. 7 the REMA extractions and accuracy assessment. (a) REMAs identified manual interpretation, (b) REMAs extracted from MMFI image, (c) REMAs extracted using the combined criteria

Accuracy assessment

Since the REMA is extracted by a threshold to convert MMFI image to actual class labels, and label all records whose MMFI values are greater than threshold by REMAs and label the reminding records as

background, it is clear that different threshold will lead to different identification accuracy. Therefore, the relative operating characteristic (ROC) was adopted to evaluate the MMFI image capacity (Wu et al., 2009). Moreover, the overall accuracy (OA) and F-value measure (Lewis and Gale, 1998) were also used. We adopted the OA measure to assess the classification accuracy performance, because it is the simplest and one of the most popular accuracy measures (Wu et al,, 2013) and is recommended for use as a primary measure for classifier performance (Liu et al. 2007). However, since pixels with background land covers dominate the study area (>99%), its accuracy largely influences the overall accuracy. To maintain the objective classification accuracy, we must ensure that small, but important, REMA areas are represented in the samples (Congalton, 1988). To this aim, we stratified randomly selected 600 REMA pixels and 1200 background pixels to evaluate the accuracy of the REMA extraction.
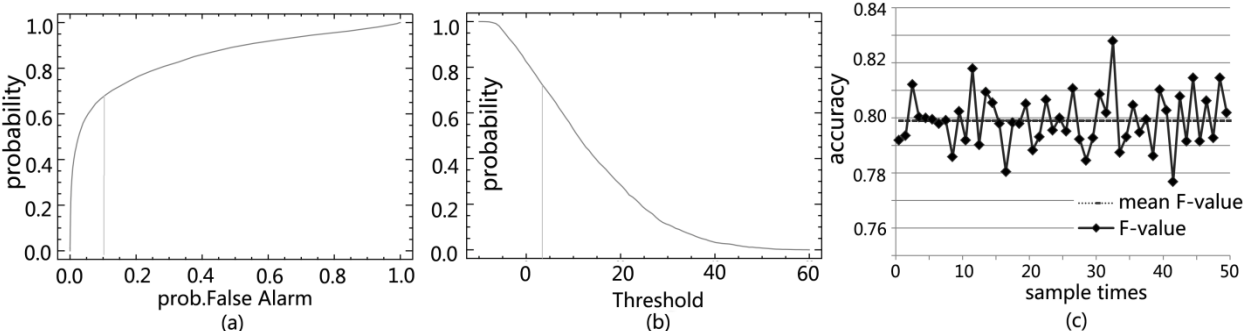
Fig.8 Accuracy evaluation with ROC and F-value measures

To define the ROC, Fig. 8a plots the probability of detection on the vertical axis versus the probability of false alarm on the horizontal axis for each of the 200 scenarios, and Fig. 8b illustrates the threshold versus the probability of detection. The AUC of MMFI is 0.846, indicating that MMFI is a good indicator to separate the REMA from background. It can be also observed that if the threshold t_1 equals to 3.56 (see vertical line in Fig.8b), the probability of detection and the probability of false alarm are about 70% and 10% respectively, suggesting the rationality of the selected threshold. To evaluate the stability of our method, we

generated samples for 50 times, where each time the F-value was calculated, which is plotted in Fig. 8c. The F-value varies, with the best and the worst F-value accuracy results being 82.7% and 77.7%, respectively, and an average accuracy of 79.8% with a variance of 0.9%.

Table 2 Comparison of the classification accuracy using different methods for REMA extraction

Methods	GLCM-SVM	FT-SVM	Proposed
OA (%)	86.3	86.9	88.8

To further evaluate the effectiveness of the proposed MMFI, two additional REMA extraction methods were carried out for comparison. The first is the GLCM textural features for supervised classification (Peng et al., 2013). Specifically, the principal component analysis (PCA) transformation was first carried out, and then the first PC feature was applied to extract 6 GLCM textural features, i.e. homogeneity, dissimilarity, entropy, variance, second moment, and contrast. These, together with the original spectral features were inputted to the SVM classifier for REMA extraction. The second method used for comparison is the fractal based texture for supervised classification. This method also uses the PC single band as input to the double blanket covering fractal method for extracting the fractal texture (Li et al., 2014) which are then added to the original bands and interpreted by a SVM (FT-SVM). Since the size of the moving windows plays an important role in feature extraction, we examined the moving windows of dimensions 3×3, 5×5, 7×7, 9×9, and 11×11 to determine the best classification. In the experiments, 200 REMA pixels and 400 other land cover pixels were randomly selected from the reference image for training of the GLCM-SVM and FT-SVM, and the remaining data was used for the evaluation. The SVM parameters C and γ tuned by ranges were within {e−5, e−3,…, e11} and {e−8, e−6,…, e4}, respectively. Their classification accuracies are reported in Table 2. Both the GLCM-SVM (Huang and Zhang, 2013) and FT-SVM methods produced comparable results with the proposed method. However, with the

supervised approaches, a larger number of training samples are needed to train the REMA model. In addition, the process of machine learning is always time consuming. Consequently, the proposed REMA identification method is more suitable for REMA extraction, especially for large area of REMA monitoring.

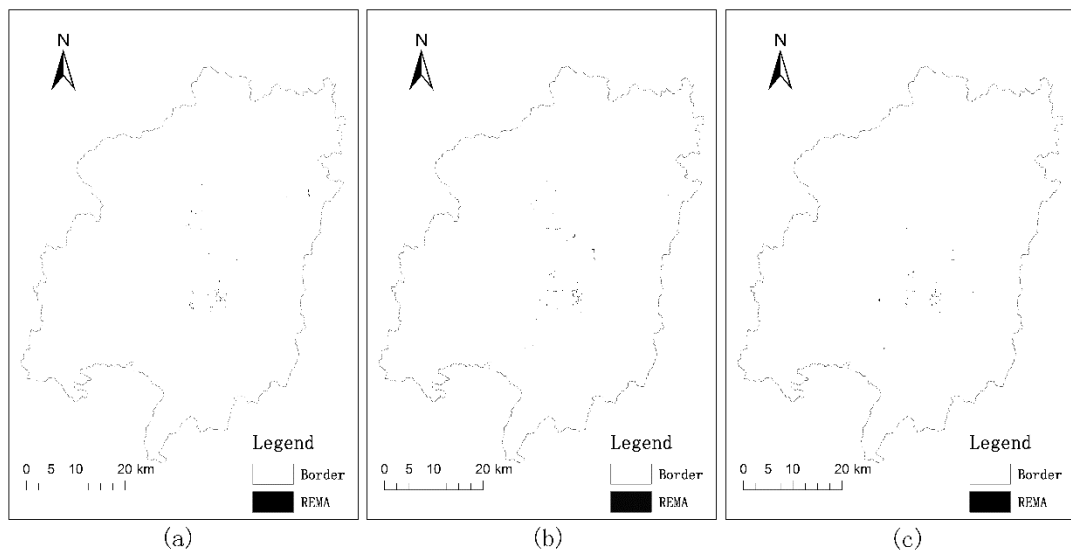The spatio-temporal distribution and changes of REMA

Fig. 9 Extracted REMAs for the three temporal images; (a) 2003, (b) 2010, and (c) 2013

The extracted REMA maps for the years 2003, 2010, and 2013 derived by the techniques mentioned above are shown in Fig. 9a, 9b, and 9c, with REMA coverage of 1.270 km^2, 1.676 km^2, and 1.213 km^2, respectively. The total REMA coverage increased from 1.27 km^2 to 1.67 km^2 between 2003 and 2010, where the newly detected REMAs cover 1.5 km^2, and the area previously identified as REMA and redefined as vegetation is 1.1 km^2, accounting for a total area of 47.87%. In contrast, there is a decrease of REMA by 0.46 km^2 from 1.67 km^2 to 1.21 km^2 between 2010 and 2013, where 0.748 km^2 was reclassified as vegetation and 0.129 km^2 as farmland. These results indicate that the desertification of land caused by mining activities has slowed down by introducing strict restrictions on mining by the Fujian provincial

government in recent years (Ministry of Land and Resources of the People's Republic of China, 2011),

and by increased effort to control soil erosion in this area.

Conclusion

This paper proposes a fully automatic method for REMA extraction from LANDSAT imagery. Our

aim is to extract the REMA automatically yet effectively without sample collection and machine learning,

such that it is suitable for REMA extraction and dynamic monitoring over large areas. Three temporal

images were obtained for REMA extraction; the results using the proposed extraction method demonstrate

that MMFI increases the effectiveness of REMA extraction, obtaining a classification accuracy of 88.8%.

This is achieved by the method's improved ability to identify roads and bare land with similar spectral

responses to those of REMAs. We compared our method with the GLMC and fractal based methods, which

have proven their reliability and good performance in mining classification. The comparison demonstrates

that the proposed method outperforms these two widely used methods, although the improvements of the

proposed method over GLMC-SVM and FT-SVM was moderate, an increase of 1.9% and 2.5%,

respectively, in terms of overall accuracy. Our method, however, can extract the REMA automatically yet

effectively without sample collection and machine learning, providing a more suitable option for REMA

extraction, especially for REMA monitoring over large areas.

Acknowledgements

References

Beneditsson, J. A., Pesaresi, M., Arnason, K., 2003. Classification and feature extraction for remote sensing images from urban area based on morphological transformations. *IEEE Transaction on geosciences and remote sensing*, 41 (9): 1940–1949.

Chen, X., Warner, T.A., Campagna, D.J., 2007. Integrating visible, near-infrared and short-wave infrared hyperspectral and multispectral thermal imagery for geological mapping at Cuprite, Nevada. *Remote Sensing of Environment,* 110(3): 244–256.

China National Bureau of Statistics, 2010. China statistical yearbook 2009, Beijing, *China Statistics press*, pp.1031–1032.

Congalton, R.G., 1988. A comparison of sampling schemes used in generating error matrices for assessing the accuracy of maps generated from remotely sensed data. *Photogrammetric Engineering and Remote Sensing,* 54 (5): 593–600.

Crosta, A. P, Moore, J. M., 1989. Geological mapping using Landsat thematic imagery inalmeria province, southeast Spain. *I International Journal of Remote Sensing*, 10 (3): 505–514.

Fauvel, M., Beneditsson, J. A., Chanussot, J., Sveinsson J. R., 2008. Spectral and spatial classification of hyperspectral data using SVMs and morphological profiles. *IEEE Transaction on geosciences and*

remote sensing, 46 (11): 3804–3814.

Huang, X., Zhang, L. P., 2011. A multidirectional and multi-scale morphological index for automatic building extraction from multispectral GeoEye-1 imagery. *Photogrammetric Engineering and Remote Sensing,* 77(7): 721–732.

Huang X., Zhang L., 2012, Morphological building/shadow index for building extraction from high-resolution imagery over urban areas. *IEEE Journal of Selected Topics in Applied Earth Observations and Remote Sensing,* 5 (1): 161–172.

Huang X., Zhang L., 2013. An SVM ensemble approach combining spectral, structural, and semantic features for the classification of high-resolution remotely sensed imagery. *IEEE Transactions on Geoscience and Remote Sensing*, 51(1): 257-272.

Huang X., Lu Q., Zhang L., Antonio P., 2014. New post-processing methods for remote sensing image classification: a systematic study. *IEEE Transactions on Geoscience and Remote Sensing*, 52(11): 7140-7159.

Jin, X. Y, Davis, C. H., 2005. Automated building extraction from high-resolution satellite imagery in urban areas using structural, contextual, and spectral information. *EURASIP Journal on Applied Signal Processing,* 14, 2196–2206.

Kapur, J. N, Sahoo, P. K, Wong, A. K. C.,1985. A new method of gray level picture thresholding using the entropy of the histogram. *Computer Vision, Graphics and Image Processing,* 29 (85): 273–285.

Lewis, D., Gale, W., 1998. Training text classifiers by uncertainty sampling. Proceedings of the Seventeenth Annual International ACM SIGIR Conference on Research and Development in Information, New York, NY. 73–79.

Levine, M. D, Nazif, A. M., 1985. Dynamic measurement of computer generated image segmentation. *IEEE Transactions on Pattern Recognition Analysis and Machine Intelligence,* 7(2): 155–164.

Li, H., Wu, L., Liu, X., 2014. Change detection of ground surface environment in rare earth mining area based on multitemporal remote sensing : a case study in Lingbei rare earth mining area. *Journal of China University of mining & technique (in Chinese with English abstract)*, 43 (6): 1087–1094.

Li N., Frei, M., Altermann, W., 2009. Improvement on Lithologic Classification Using Rule-based System. *Proceedings of the 20th Annual Meeting of the Geological Remote Sensing Group (GRSG)*, 15–17 December, London, UK.

Li X., Chen Z., Chen Z., Zhang Y., 2013. A human health risk assessment of rare earth elements in soil and vegetables from a mining area in Fujian Province, Southeast China. *Chemosphere*, 93(6): 1240–1246.

Liu, C., Frazier, P., Kumar, L., 2007. Comparative Assessment of the Measures of Thematic Classification Accuracy. *Remote Sensing of Environment,* 107(4): 606–616.

Mars, J. C, Rowan, L. C., 2011. Spectral assessment of new ASTER SWIR surface reflectance data products for spectroscopic mapping of rocks and minerals. *Remote Sensing of Environment,* 114 (9): 2011–2025.

Mao, L., Mo, D., Li, M., Zhou, K., Yang, J., Guo, W., 2011. The rare earth element compositions of sediments from the loess tableland in the Liyang Plain, southern China: implications for provenance and weathering intensity. *Environment Earth Science,* 62 (8): 1609–1617.

Ministry of Land and Resources of the People's Republic of China (MLR), 2011. assessed March 1: http://www.mlr.gov.cn/kczygl/kcbh/

Myint, S. W., Lam, N. S. N., Tyler, J., 2004. Wavelets for urban city spatial feature discrimination:

comparisons with fractal, spatial autocorrelation and spatial co-occurrence approaches. *Photogrammetric Engineering and Remote Sensing,* 70 (7): 803–812.

Olías, M., Cerón, J.C., Fernández, I., Rosa, J. D., 2005. Distribution of rare earth elements in an alluvial aquifer affected by acid mine drainage: the Guadiamar aquifer (SW Spain). *Environment Pollution,* 135 (1): 53–64.

Ouma, Y. O., Ngigi, T. G., Tateishi, R., 2006. On the optimization and selection of wavelet texture for feature extraction from high-resolution satellite imagery with application towards urban-tree delineation. *International Journal of Remote Sensing*, 27(1): 73–104.

Ostu, N., 1979. A threshold selection method from gray-level histograms. *IEEE Transactions on systems, man and cybernetics,* 9(1):62–66.

Peng, Y., He, G., Cao, H., 2013. Extraction of rare earth mining areas using objects-oriented classification approach based on texture characteristics. *Science Technology and Engineering (in Chinese with English abstract)*, 13 (19): 5590–5596.

Pour, A. B, Hashim, M., 2012. The application of ASTER remote sensing data to porphyry copper and epithermal gold deposits. *Ore Geology Reviews*, 44 (1): 1–9.

Pesaresi, M., Benediktsson, J.A. 2001. A new approach for the morphological segmentation of high-resolution satellite imagery. *IEEE Transaction on geosciences and remote sensing*, 39 (2): 309–320.

Rowan, L. C., Mars, J. C., 2003. Lithologic mapping in the Mountain Pass, California area using Advanced Spaceborne Thermal Emission and Reflection Radiometer (ASTER) data. *Remote Sensing of Environment,* 84 (3): 350–366.

Sabins, F. F., 1999. Remote sensing for mineral exploration. *Ore Geology Reviews,* 14(99): 157–183.

Wu, B., Chen, C., Mohand, K. T,. Sun, L., 2013. A comparative evaluation of filter-based feature selection methods for hyper-spectral band selection. *International Journal of Remote Sensing*, 34 (22): 7974–7990.

Wu, B, Huang, B, Fung, T., 2009. Projection of land use change patterns using kernel logistic regression. *Photogrammetric Engineering and Remote Sensing,* 75 (8): 971–979.

Yu, L., Porwal A., Holden E-J., Dentith M. C., 2011. Suppression on vegetation in multispectral remote sensing images. *International Journal of Remote Sensing*, 32 (22): 7343–7357.

Yu, L., Porwal, A., Holden, E-J., Dentith, M. C., 2012. Towards automatic lithological classification from remote sensing data using support vector machines. *Computers & Geosciences,* 45 (6): 229–239.